On the baroclinic response of supercritical topography to an oscillating tide: LES results

Masoud Jalali, Presenting Author and Sutanu Sarkar

Department of Mechanical and Aerospace Engineering,
University of California San Diego
mjalalib@ucsd.edu

Abstract

Steep topography on the ocean bottom, when underneath an oscillating tide, is not only associated with significant internal wave generation at the tidal frequency but also nonlinear flow features, large overturns and turbulent flow. Here, we investigate the internal wave dynamics and turbulence at an isolated steep obstacle using a three-dimensional, high-resolution large eddy simulation (LES). An obstacle with a smoothed triangular shape having a supercritical slope above a critical slope is considered as a laboratory-scale model of a two-dimensional ocean ridge. Downslope jets with intensified velocity from in the supercritical region. Later on, during the flow reversal phase, this jet encounters upward flow and creates a rebounding jet that distorts the density isopycnals as well as a transient lee wave above the obstacle. Primary mechanisms responsible for turbulence are shear in the jet and convective instabilities arising from steepened isopycnals followed by wave breaking. There is also turbulence generation from resonance in the near-critical boundary flow.

1 Introduction

Oscillating barotropic flow of a density stratified fluid over bottom topography is responsible for the generation of internal gravity waves. A fraction of the energy converted from the oscillating tide to the baroclinic wave field dissipates through turbulence in the vicinity of the topography and this fraction can be significant. The fractional energy loss depends strongly on the topographic geometry, the stratification and the amplitude of the oscillatory forcing. Steep submarine topography not only enhances the generation of topographic internal waves, but also presents a site for intensified local turbulence as found in observational studies at the Hawaiian Ridge (Rudnick and Co-authors, 2003) and Luzon Strait(Alford and Co-authors, 2015).

Numerical simulations show nonlinear flow features at large obstacles (Klymak et al., 2008) with low value of excursion number, Ex, as well as small obstacles with $O(1)$ values of Ex (Jalali et al., 2014). Consider a barotropic tide that oscillates with frequency Ω and whose velocity has amplitude U_0. The excursion number defined by $Ex = U_0/\Omega l$ is the ratio of fluid displacement during a cycle of the barotropic tide to the topographic length scale, l. Nonlinear effects are possible when the value of excursion number is $O(1)$, based on the dynamically relevant velocity and length scales. For small obstacles, Ex is dynamically relevant but for tall obstacles ($Fr = U_0/Nh << 1$) an inner excursion number is dynamically relevant (Winters and Armi, 2013). N is a characteristic value of the background buoyancy frequency and h is a characteristic height. Because of the difference between wave-driven turbulence and boundary layer turbulence, the magnitudes of mixing and dissipation are not well captured by standard parameterizations such as Mellor and Yamada (1982).

Steep topography can be identified with the criticality parameter, $\epsilon = \tan\beta/\tan\theta$, which is the ratio of the topographic slope angle, $\tan\beta$, to the characteristic wave propagation angle $\tan\theta = \sqrt{(\Omega^2 - f^2)/(N^2 - \Omega^2)}$. Supercritical slopes ($\epsilon > 1$) and near-critical slopes ($\epsilon \simeq 1$) have local turbulence. Legg and Klymak (2008) identified transient hydraulic jump-like features that occur during the maximum barotropic velocity phase and overturned isopycnals in the flow reversal phase for supercritical topography. This behavior is analogous to breaking lee waves in steady flow over obstacles. Recent observations by Alford et al. (2014) at a transect across the Kaena Ridge present evidence for lee wave formation and breaking at supercritical topography. Lee wave breaking has also been observed in Luzon Strait by Alford and Co-authors (2015) and in numerical simulations of Buijsman et al. (2012); Jalali and Sarkar (2014); Jalali et al. (2015).

Critical slopes with $\varepsilon \approx 1$ have substantial near-bottom intensification of velocity owing to resonance in the baroclinic response. When Re_s is low, there is a laminar boundary layer (Gostiaux and Dauxois, 2007; Zhang et al., 2008) while, at high Re_s ($Re_s > 100$), there is a thickened boundary layer with cyclical overturns (Gayen and Sarkar, 2010; Lim et al., 2010) and turbulence. Here, Re_s is the Reynolds number based on the Stokes boundary layer thickness.

Sites like Luzon Strait have near-critical ($\epsilon \approx 1$) regions at the hillside as well as supercritical slope angle near the hilltop. This motivates the present three-dimensional, high-resolution large eddy simulation (LES) to study flow over a simplified model of real topographies with variable steepness. The key nondimensional parameters, except for the Reynolds number, are similar between the model and oceanic sites, including: the slope criticality, the Froude number, the excursion number, the ratio of topography height, h_o, to width, l_o, and the ratio of topographic height to the depth of the ocean, H. The baroclinic response in this simplified model will help better understand processes at realistic ocean topography.

2 Formulation and Framework

2.1 Governing Equations

The Navier-Stokes equations listed below are numerically solved using LES in a body conforming grid and under the Boussinesq approximation in a non-rotating environment:

$$\nabla \cdot \mathbf{u} = 0 \tag{1a}$$

$$\frac{D\mathbf{u}}{Dt} = -\boldsymbol{\nabla} p^* + F_b(t)\mathbf{i} + \frac{1}{Re}\nabla^2\mathbf{u} - B\rho^*\mathbf{k} - \nabla\cdot\tau \tag{1b}$$

$$\frac{D\rho^*}{Dt} = \frac{1}{Re\ Pr}\nabla^2\rho^* + w\frac{d\rho^b}{dz} - \nabla\cdot\lambda\ . \tag{1c}$$

Here, u, v, and w denote velocity in streamwise (x), spanwise (y), and vertical (z) directions, respectively. Bold letters stand for vector/tensor variables. ν is the molecular viscosity, κ is the thermal diffusivity, and ρ is the density.

The non-dimensional parameters are the Reynolds number $Re \equiv \frac{l_{ex}U_0}{\nu} = \frac{U_0^2}{\Omega\nu}$, buoyancy parameter $B \equiv -g\frac{d\rho_d^b}{dz_d}|_\infty \frac{1}{\rho_0\Omega^2} = \frac{N^2}{\Omega^2}$, and Prandtl number $Pr \equiv \frac{\nu}{\kappa}$. Here, p^* and ρ^* stand for the deviation from the background pressure and density, respectively. F_b is a

barotropic forcing term. In this equation, τ is the subgrid-scale (SGS) stress tensor and λ is the SGS density flux. The popular dynamic Smagorinsky model (Zang et al., 1993) is used to calculate the SGS stress tensor and the SGS density flux.

2.2 Problem Setup

An oscillating tide over a two dimensional obstacle, Figure 1, is studied using a fully non-linear, three-dimensional simulation. Background thermal stratification with a constant buoyancy frequency, N, is considered while the bottom surface is assumed adiabatic. The background barotropic current, $U(x)sin(\phi)$ where ϕ is the tidal phase, is forced by an imposed horizontal pressure gradient. Table 1 gives the key parameters of the simulations.

A laboratory-scale model is used to achieve sufficient resolution for the turbulent features at the slope as well as off-slope lee wave breaking. Both horizontal and vertical length scales are decreased 100 times compared to oceanic examples. Approximately 25% of the topographic width has near-critical slope. The critical regions are placed on the flanks close to the flat bottom between $x = \pm 64m$ and $x = \pm 44m$. The supercritical region is closer to the hill crest between $x = \pm 36m$ and $x = \pm 16m$ covering 25% of the horizontal length of topography, as shown in Figure 1. Supercritical slope angle is $\beta_2 = 14.68°$ compared to the near-critical slope angle of $\beta_1 = 7.34°$.

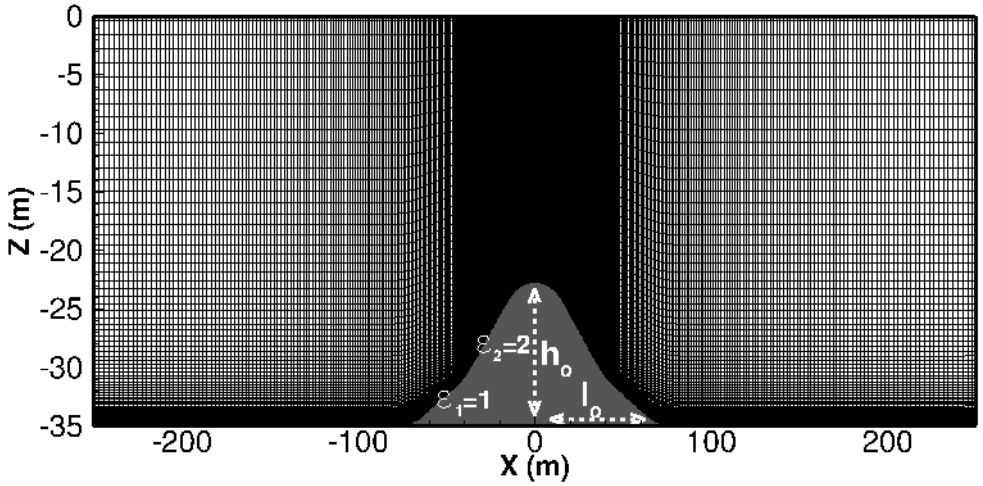

Figure 1: The body fitted computational domain, the grid has been shown partially with one of every three horizontal and vertical grid points.

Table 1: Key dimensional and nondimensional parameters of the simulation. The domain has streamwise length, $L_x = 50\ m$, height, $L_z = 35\ m$, and spanwise length, $L_y = 15\ m$. Topography length, $L_0 = 2l$, is 160 m and height, h_0, is 12.32 m. The critical angle is $\beta_1 = \theta = 7.34°$ while the supercritical slope angle is $\beta_2 = 14.68°$ and the tidal frequency is $\Omega = 0.01406\ s^{-1}$.

$U_0[ms^{-1}]$	$\nu[m^2s^{-1}]$	$N^2[s^{-2}]$	Ex	ε_1	ε_2	Re	Fr	Ny	Nz	Nx
0.1	5e-5	0.0121	0.09	2	1	17781	0.073	64	257	1281

3 Baroclinic Response

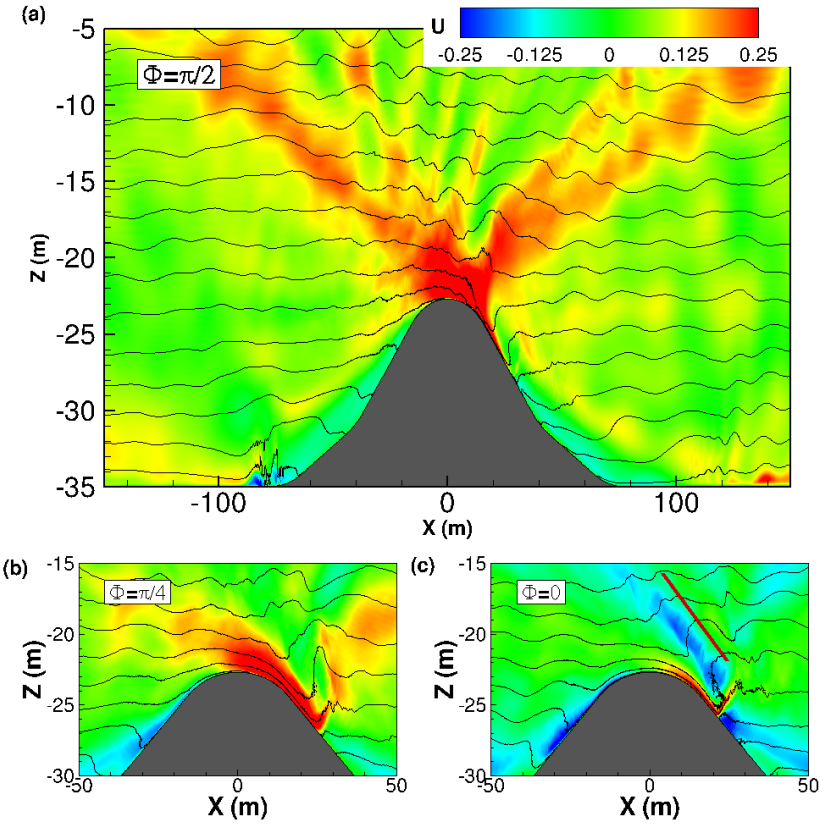

Figure 2: Snapshots of zonal velocity and density isopycnals at different phases of the tidal cycle: (a) maximum barotropic velocity ($\phi = \pi/2$) (b) $\phi = \pi/4$, and (c) reversal of the barotropic tide through the zero velocity point ($\phi = 0$). The red line passes through crests of a transient lee wave.

The flow exhibits internal wave beams, intensified boundary flow and tall overturns. Figure 2 compares the baroclinic response at different phases of barotropic velocity. Figure 2 (a) depicts the zonal velocity at the phase $\phi = \pi/2$ with maximum positive (rightward) velocity. The upward propagation of the fundamental wave beams as well as harmonics and interharmonics are evident in the baroclinic response above the obstacle. The beams become less distinct and more asymmetric with increasing Ex as discussed in Jalali et al. (2016). There are also two beams traveling downwards from the supercritical region. The maximum velocity at the obstacle peak is substantially larger than the barotropic velocity, approximately by a factor of 3. The intensified velocity also extends a short distance down the right (lee) flank. That feature is the initiation of an intense downslope jet which is clearly visible in panel (b) at the phase $\phi = \pi/4$. Formation of the downslope jet in the lee of an obstacle is a signature of supercritical obstacles.

Figure 2 (c) depicts the flow dynamics at the zero-velocity phase ($\phi = \pi$). At this point, the barotropic velocity reverses from positive to negative. The jet continues to have downward momentum owing to fluid inertia and collides with the baroclinic flow that travels upslope from below, and this interaction creates a *rebounding jet* perpendicular to the slope of the topography. The lee wave above the rebounding jet leads to overturned isopycnals. The phase line in red that passes through crests of the lee wave is observed

to make an angle of $\alpha_{obs} = 15.65°$ with the horizontal. The inner length scale, l_{in}, of the topography is relevant to lee wave generation, not the entire obstacle length. The inner length scale is estimated by the point at which the jet rebounds from the obstacle leading to $l_{in} = 21$ m. According to the linear theory of lee wave generation,

$$\alpha_{th} = \sin^{-1} \frac{U_0 k}{N} = \sin^{-1} \frac{U_0 2\pi}{l_{in} N} \tag{2}$$

Equation (2) leads to the linear theory estimate of $\alpha_{th} = 15.75°$ which is close to the observed value of 15.65°.

4 Turbulence Mechanisms

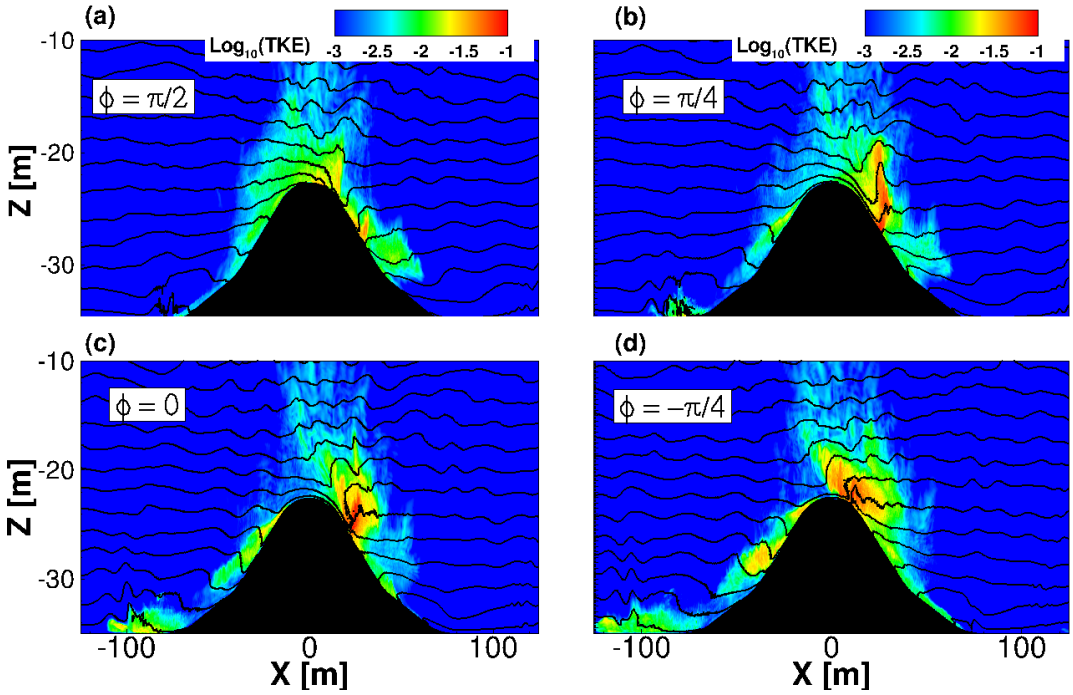

Figure 3: Snapshots of logarithmic-scale contours of turbulence kinetic energy(TKE) with the density isopycnals at different phases of: (a) $\phi = \pi/2$ (b) $\phi = \pi/4$ (c) $\phi = 0$ and (d) $\phi == \pi/4$.

The previous section discussed the evolution of the downslope jet and lee wave. Figure 3 shows the corresponding turbulent kinetic energy (TKE) contours in log scale at different phases of a half-cycle. Panel (a) shows the intensified flow that propagates as a downslope jet generates boundary layer turbulence due to its shear. Panel (b) displays the progression of the jet has depressed the isopycnals at the slope which then rebound to form a weakly stratified region corresponding to incipient wave breaking. A tall patch of TKE is present in this weakly stratified region. Panel (c) shows that, as the tidal velocity relaxes towards zero, the wave grows and breaks. The resulting patch of TKE is then advected over the topography by the barotropic flow and the baroclininc velocity of the wave beams as shown in panel (d).

The two significant contributors to turbulence in this problem are shear in the downslope jet and the convective instability of nonlinearly evolving lee waves. However, there are

also other contributors present in this setting, though not as significant. For example, the baroclinic response at the near-critical slope leads to resonance and intensification of the near-bottom velocity. As a result, turbulence at the critical region can be seen on the right side flank at $\phi = -\pi/4$; however it is not as prominent as in Gayen and Sarkar (2010); Jalali et al. (2014) where the critical slope region was adjacent to subcritical slopes allowing resonant generation of strong internal wave beams that propagated away. In the present problem, the strong baroclinic response at the adjacent supercritical region and the downward internal wave beams from the critical points at the top of the ridge restrict the velocity intensification at the critical slope. Therefore, critical-slope turbulence is less prominent in the present problem. Additional contributors to TKE in the simulation are turbulence patches that develop due to the shear in the superharmonics and downward beams as well as when the downward beam interacts with the bottom boundary.

5 Conclusion

An accurate numerical simulation of an isolated model ridge with both critical and supercritical slope has helped understand turbulent processes operative at steep topography in the deep ocean. Several mechanisms are found to be responsible for turbulence near the ridge top, including downslope jets and breaking lee waves during flow reversal. We also find contributions to TKE from critical slope boundary layers, internal wave beams, superharmonics and downward beams. We note that the present simulation is a specific geometry and, therefore, further investigation is necessary to examine different geometries of the model ridge.

References

Alford, M. H. and Co-authors (2015). The formation and fate of internal waves in the South China Sea. *Nature*, 521:0028–0836.

Alford, M. H., Klymak, J. M., and Carter, G. S. (2014). Breaking internal lee waves at Kaena Ridge, Hawaii. *Geophys. Res. Lett.*, 41:906–912.

Buijsman, M., Legg, S., and Klymak, J. M. (2012). Double-Ridge Internal Tide Interference and Its Effect on Dissipation in Luzon Strait. *J. Phys. Oceanogr.*, 42:1337–1356.

Gayen, B. and Sarkar, S. (2010). Turbulence During the Generation of Internal Tide on a Critical Slope. *Phys. Rev. Lett.*, 104:218502.

Gostiaux, L. and Dauxois, T. (2007). Laboratory experiments on the generation of internal tidal beams over steep slopes. *Phys. Fluids*, 19:028102.

Jalali, M., Chalamalla, V. K., and Sarkar., S. (2015). On the accuracy of overturn-based estimates of turbulent dissipation at rough topography. *J. Phys. Oceanogr.*, submitted.

Jalali, M., Rapaka, N. R., and Sarkar, S. (2014). Tidal flow over topography: effect of excursion number on wave energetics and turbulence. *J. Fluid Mech.*, 750:259 – 283.

Jalali, M. and Sarkar, S. (2014). Turbulence and dissipation in a computational model of Luzon Strait. *Bulletin of the American Physical Society*, 59.

Jalali, M., VanDine, A., Chalamalla, V. K., and Sarkar., S. (2016). Oscillatory stratified flow over supercritical topography: wave energetics and turbulence. *Computers & Fluids*, submitted.

Klymak, J. M., Pinkel, R., and Rainville, L. (2008). Direct breaking of the internal tide near topography: Kaena Ridge, Hawaii . *J. Phys. Oceanogr.*, 38:380–399.

Legg, S. and Klymak, J. (2008). Internal hydraulic jumps and overturning generated by tidal flows over a tall steep ridge . *J. Phys. Oceanogr.*, 38:1949–1964.

Lim, K., Ivey, G. N., and Jones, N. L. (2010). Experiments on the generation of internal waves over continental shelf topography. *J. Fluid Mech.*, 663:385–400.

Mellor, G. L. and Yamada, T. (1982). Development of a turbulence closure model for geophysical fluid problems. *Rev. Geophys. Sp. Phys.*, 20:851.

Rudnick, D. L. and Co-authors (2003). From tides to mixing along the Hawaiian Ridge. *Science.*, 301:355–357.

Winters, K. B. and Armi, L. (2013). The response of a continuously stratified fluid to an oscillating flow past an obstacle. *J. Fluid Mech.*, 727:83–118.

Zang, Y., Street, R. L., and Koseff, J. R. (1993). A dynamic mixed subgrid-scale model and its application to turbulent recirculating flows . *Phys. Fluids A*, 5(12):3186–3196.

Zhang, H. P., King, B., and Swinney, H. L. (2008). Resonant Generation of Internal Waves on a Model Continental Slope. *Phys. Rev. Lett.*, 100:244504.